



Ultra-high current density water management in polymer electrolyte fuel cell with porous metallic flow field

A.K. Srouji^{a,c}, L.J. Zheng^{b,c}, R. Dross^d, A. Turhan^c, M.M. Mench^{c,e,*}

^a Department of Energy and Mineral Engineering, The Pennsylvania State University, University Park, PA 16801, USA

^b Department of Mechanical and Nuclear Engineering, The Pennsylvania State University, University Park, PA 16801, USA

^c The Electrochemical Energy Storage and Conversion Laboratory, Department of Mechanical, Aerospace and Biomedical Engineering, University of Tennessee, Knoxville, TN 37996, USA

^d Nuvera Fuel Cells Inc., Billerica, MA 01821, USA

^e Energy and Transportation Science Division, Oak Ridge National Laboratory, Oak Ridge, TN 37831, USA

HIGHLIGHTS

- Stable operation up to 90 °C is demonstrated with the open metallic element architecture and high current density.
- Flooding is not limiting at high current, operation is limited by dry-out.
- Net water drag measurement reveals that back diffusion controls cell operation.

ARTICLE INFO

Article history:

Received 17 November 2012

Received in revised form

20 February 2013

Accepted 20 March 2013

Available online 3 April 2013

Keywords:

Fuel cell

Water management

High current

Porous flow field

Dry out

Back diffusion

ABSTRACT

Anode dry-out is the main mechanism identified to limit operation in an open metallic element (OME) PEFC. The fundamental water transport mechanisms in the OME PEFC were examined in order to engineer further improved performance and higher temperature operation required for efficient heat rejection. Specifically, the net water drag (NWD) was measured over a range of conditions and analyzed with respect to electrochemical impedance spectroscopy and performance. As the cell operating temperature was increased, the effect of back diffusion was reduced due to the diminishing liquid water content in the cathode catalyst layer, and at critical liquid water content, anode dry-out was triggered primarily through electro-osmotic drag. Addition of cathode humidity was shown to promote high temperature operation mostly due to improved water back diffusion. The same mechanism can be achieved by creating a pressure differential across the membrane, with higher pressure on the cathode side. Stable operation was demonstrated at 90 °C using a polymer electrolyte membrane. Real time NWD measurements during transient anodic dry-out conditions were consistent with gradual membrane dehydration. The trade-off between liquid water overshadowing cathode catalyst sites and its contribution in promoting back diffusion is a key factor in systems with anode dry-out limited operation.

© 2013 Elsevier B.V. All rights reserved.

1. Introduction

Growing concerns about preserving the environment and finding sustainable sources of energy have brought hydrogen to the forefront of clean energy carriers. Polymer electrolyte fuel cells (PEFCs) are prominent candidates as power generating devices,

converting energy stored in hydrogen gas into useable electric power. PEFCs operating on renewable hydrogen are of particular interest to the automotive industry since they are highly efficient, with zero-emissions, and operate at high-power density. The next decade will play a major role in commercializing fuel cell vehicles as most major car manufacturers plan to enter early commercialization by 2015 [1–4]. Continual improvement in performance, cost, and durability is required for successful market implementation.

In PEFCs, the cathode performance is often limiting [5,6]. This is due to both the slower oxygen reduction reaction (ORR) kinetics at the cathode compared to fast hydrogen oxidation reaction (HOR) at the anode, and mass transport limitation caused by limited oxygen

* Corresponding author. The Electrochemical Energy Storage and Conversion Laboratory, Department of Mechanical, Aerospace and Biomedical Engineering, University of Tennessee, Knoxville, TN 37996, USA. Tel.: +1 865 974 6751; fax: +1 865 974 5274.

E-mail addresses: mmench@utk.edu, matthewmench@gmail.com (M.M. Mench).

diffusion and liquid water flooding at high current density [5–9]. The conventional bias in the design of fuel cell flow fields using alternating channel/land configuration is a result of the functional requirements of a flow field [10–17]. Channels distribute reactants and remove products, while lands are needed to provide adequate support, compression, and conduction of heat and current.

Various methods for excess water removal have been identified, and can involve modification of different components. Generally speaking, the modification can be in the flow field design, operating parameters, or in the soft materials such as diffusion media (DM), microporous layer (MPL) or catalyst layer (CL). Compared to a conventional parallel channel/land (C/L) design, a properly designed serpentine flow field at the cathode removes more residual water due to increased pressure drop and enhanced convective forces at the same stoichiometry [18,19], while an interdigitated flow field forces reactant flow convectively toward the active layer [20]. Modification of the C/L flow field material properties has also been proposed. Hydrophilic treatment of channel walls enhances liquid suction from locations under the land while polytetrafluoroethylene (PTFE) treatment of the C/L interface was demonstrated to increase water storage in the DM and promote flooding [21,22]. A C/L flow field made of porous carbon was devised to distribute gas in a conventional way and to act as a passive wick for water removal and redistribution of humidity [23]. Component level modifications have also been proposed to mitigate flooding. For example, it was shown that DM with relatively low in-plane gas permeability accounts for a greater amount of liquid water retention under the lands. An increase in PTFE content in the DM and MPL was shown to promote removal of water from the cathode, but an excess amount of PTFE leads to increased electrical contact resistance and reduction in performance [24,25]. In recent studies, DMs were altered by laser perforation to investigate the effect of structural change on water management [26–28]. Results indicated that perforations acted as water reservoir pools and redistributed water in low humidity conditions. At high current or wet conditions performance was poor. Even though the aforementioned strategies differ, they all deal with conventional architecture fuel cell consisting of alternating channel and lands. As some of them improve water removal and enhance performance, the main limit in typical operation is still due to flooding and mass transport at the cathode, an inherent characteristic of the channel land bias.

Porous metal and metallic mesh fuel distributors have been suggested for direct methanol fuel cells [29–34], and an improvement in performance is noted compared to conventional flow fields caused by improved methanol distribution and CO₂ removal. In PEFC, Kumar et al. modeled the performance of a multi-parallel flow field and the effect of filling the rectangular channels with porous metal of different permeability. The addition of porous metal in the rectangular channels leads to improved performance, and more importantly to a more uniform local current distribution. The highest simulated current density was 842 mA cm⁻² [35]. Tsai et al. examined the effect of the location of manifolds in a porous metal flow field fuel cell on fuel distribution and concluded that dividing the metal foam into multiple regions and using multiple inlets effectively increases the gas distribution and utilization rate [36].

A single cell with an open metallic element (OME), designed and developed by Nuvera Fuel Cells Inc (Billerica, MA), was tested at 60 °C in our previous work, and compared to a conventional parallel C/L architecture cell [37,38]. Results showed that mass transport limitation was drastically reduced in the OME cell. No sign of flooding was visible up to 3 A cm⁻². This was attributed to the elimination of conventional lands that usually overshadow electrode active area, trap water inside the cell, and block reactant access to the CL. Unlike an interdigitated flow field, in which

through plane convection promotes water removal under land segments, the mode of through plane transport in the OME architecture is diffusion [38]. A cross sectional schematic representing gas and liquid-phase direct flow in an OME architecture cell is presented in Fig. 1a.

Part of the water introduced in the humidified reactant streams crosses the membrane electrode assembly (MEA), and contributes to electrolyte-phase hydration. The ORR at the cathode is another source of water. Water is also moved from the anode to the cathode side of the membrane via electroosmotic drag induced by proton transport. This is due to water forming a hydration shell around a proton, or hydrodynamic pumping due to ionic and hydration shell movement [39–41]. Because electroosmotic drag affects water management in a fuel cell, it has a local and general contribution to the performance and durability. A local dry out on the anode side of the membrane can be induced by electroosmotic drag. This affects the conductivity of the membrane and therefore increases ohmic resistance and heat generation. Both water generation and

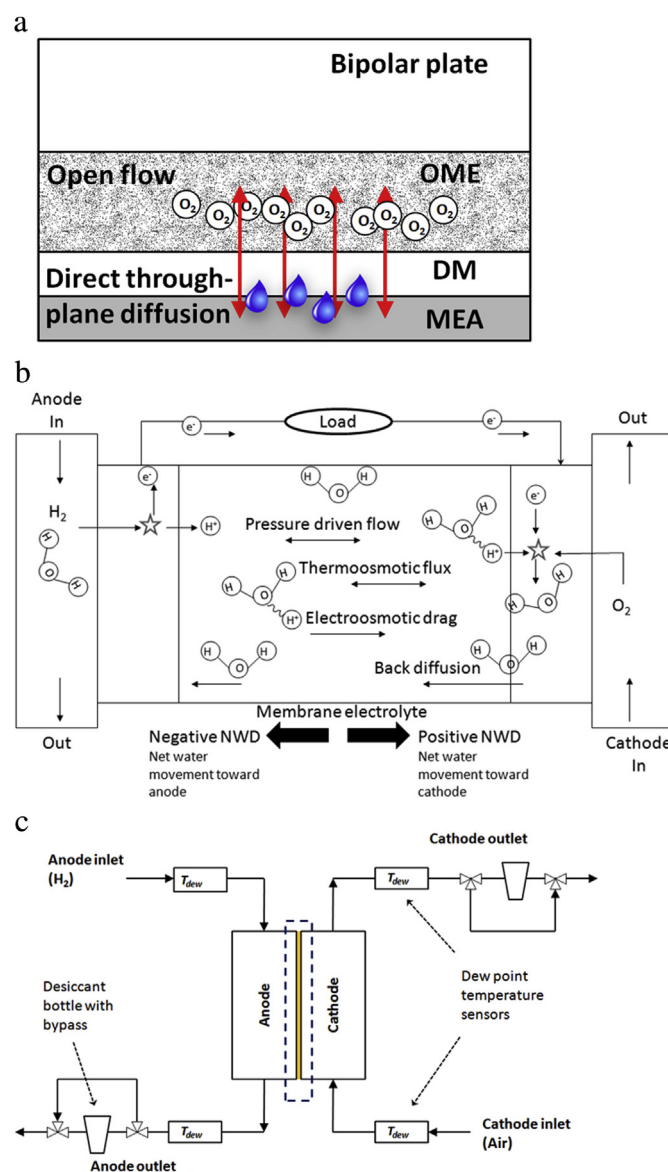


Fig. 1. a) Cross section of cathode side showing OME and improved mass transport (not to scale), b) through-plane water transport in a PEFC and net water drag (NWD), c) schematic representation of PEFC with in-line dew point temperature sensors and water desiccant bottles for live and average water measurement, respectively.

electroosmotic drag contribute to water accumulation in the cathode side of the MEA. Even though high water content in the cathode ionomer improves proton transport, the slight excess will result in reduced performance due to flooding and water film resistance over the electrochemically active area. Also, low water content in the ionomer phase of the cathode electrode is detrimental to charge transport and therefore performance. The multiple directions of water transport across the membrane are represented in Fig. 1b. The transport of water to the cathode in most cases creates a concentration gradient across the membrane. When the water concentration on the cathode side is high enough, water can move from the cathode toward the anode compartment via back diffusion. The separate measurement and estimation of electroosmosis and diffusion rates are possible [42–46]. Pressure gradients between the two gas compartments (across the membrane) also affect net water transport direction. It has also been demonstrated that temperature gradients across the membrane contribute to the movement of water via thermo-osmosis [47–51]. The combined effect during typical fuel cell operating conditions dictates the overall direction of water transport and potential for anode dry-out, and is referred to as the effective or net water drag (NWD). NWD is positive for a net flux toward the cathode and negative if the net flux is toward the anode.

PEFC stack operation at elevated temperature is desirable to reduce heat exchanger size and load. The DOE technical target for the year 2017 requires automotive stacks to operate and reject heat at a specific rate per degree difference between the stack coolant out temperature and ambient temperature ($Q/\Delta T = 1.45 \text{ kW}^\circ\text{C}^{-1}$) [52]. Although previous work has shown the OME design can operate at extremely high current at reasonable voltage, it was demonstrated at only 60 °C. The motivation of this study is therefore to extend the operating temperature window to higher temperatures suitable for automotive operation [53,54], while using conventional type polymer electrolyte membrane. In this work, we employ a single cell with open metallic element (OME) designed and built by Nuvera Fuel Cells (Billerica, MA) and investigate the limits of operation and net water drag at ultra-high current density as a function of temperature, to understand the mechanism that limits performance at increased temperature and engineer the system to enable stable high temperature operation up to 90 °C. Unlike trying to improve water evacuation in conventional C/L architecture, efforts in improving water retention are addressed for this specific architecture, and stable operation at ultra-high current density.

2. Experimental

2.1. Apparatus

The single cell used in this paper has a porous open metallic element (OME) flow field and an active area of 50 cm². The aspect ratio and boundary conditions are designed to match that of a full size stack cell. The anode and cathode reactant flows are operated in a counter-flow arrangement. All testing was conducted in galvanostatic mode. The membrane electrode assemblies (MEA) used were W. L. Gore, 18 μm (dry) membrane with a catalyst loading of 0.15 mg Pt cm⁻² at the anode and 0.4 mg Pt cm⁻² at the cathode. The diffusion media (DM) used on both electrodes are Sigracet 25BC by SGL Group (Wiesbaden, Germany), with a 5%wt PTFE content and a microporous layer (MPL) with 23%wt PTFE content.

An Arbin Instruments (College Station, TX) fuel cell testing station was used to control gas flow rates, back pressure and other operating parameters. The inlet cell pressure is set to desired values by controlling the throttle on the back pressure system. A stand-alone calibrated membrane-type humidification system from Fuel Cell Technologies Inc. (Albuquerque, NM) was used to humidify reactant gases as needed. Electrochemical impedance spectroscopy

(EIS) was performed using a Zahner IM6ex, by Zahner Elektrik (Kronach, Germany). The frequency was swept from 100 mHz to 5 kHz using a 50 mV amplitude signal. A schematic of the water measurement apparatus and connections is shown in Fig. 1c. Two calibrated dew point temperature sensors by Vaisala Inc (Helsinki, Finland) were used to measure the dew point temperatures of the gases exiting the anode and cathode of the OME cell, in order to compute the real time net water drag coefficient. Each sensor was followed by a three way valve capable of directing the flow to a desiccant bottle filled with Dryerite® (anhydrous CaSO₄, W.A. Hammond Drierite Co.) to condense and trap water. The cell outlet lines, sensors, and lines leading to each desiccant bottle were overheated in order to avoid any condensation in the lines before trapping the water. After water was trapped, the three way valves were switched to bypass the desiccant bottle. The bottles were then disconnected and the change in mass was recorded and attributed to the amount of trapped water. The measurement for each point with the desiccant bottle lasted between 15 and 20 min to maximize signal-to-noise ratio and reduce any error resulting from sporadic emissions of water droplets.

2.2. Operating conditions

2.2.1. Operating conditions for polarization curve

The baseline set of conditions used to evaluate a complete polarization curve are summarized in Table 1. The cell baseline operating temperature is 60 °C, with ultra high purity hydrogen at the anode, and air (breathing grade D) at the cathode. Constant anode and cathode stoichiometries of 2 were used. The anode inlet relative humidity was 53% (Dew point temperature set at 47 °C), and the cathode gas was dry (humidifier bottle bypassed). Back pressure was applied to both anode and cathode outlets such that their inlet pressures were both equal to 180 kPa absolute (1.8 bar absolute or 80 kPa gauge pressure).

2.2.2. Operating conditions for high current and increased temperature tests

Experiments to study water management as a function of increased operation temperature were all conducted at 2 A cm⁻² since performance at this point is not limited by mass transport limitations or any dry-out phenomena, and efficiency is still high enough for practical operation. It also satisfies operation at ultra-high current density which is one of the main features of the cell design being investigated [37]. Operation was initiated at 2 A cm⁻² under baseline conditions from Table 1, at 60 °C. Four specific test conditions were utilized as summarized in Table 2. Temperature was increased in steps after 1 h of steady state operation, during which ASR, EIS and water measurement were performed. Every operation at a specific temperature lasted at least an hour in order to insure a steady state was achieved if possible. Operation was eventually limited by dry out at a specific temperature. After that, the cell was reconditioned under humid conditions. Baseline operation performance was checked and tests were continued. The first modification to the baseline conditions was the increase of the cathode back pressure, from 180 kPa absolute to 240 kPa absolute, with all other

Table 1
Baseline operating conditions.

	Anode	Cathode
Cell operating temperature	60 °C	60 °C
Gas	Hydrogen	Air
Gas stoichiometry	2	2
Relative humidity	53%	Dry (humidifier bypassed)
Humidifier dew point temperature	47 °C	Dry (humidifier bypassed)
Inlet pressure (kPa, absolute)	180	180

conditions constant. After reconditioning the second modification was the addition of 50% RH to the cathode stream at 240 kPa absolute, with all other conditions constant. The third modification was the further increase of cathode humidity to 75% RH at the same inlet pressure of 240 kPa absolute. The specified RH at each operating condition was kept constant with increasing cell temperature. This was important, in that the humidifiers' dew points were increased with cell temperature in order to keep a constant relative humidity.

2.3. Net water drag calculation

2.3.1. Net water drag calculation

The net water drag (NWD) is defined as the net amount of water molecules transferred across the membrane, from anode to cathode, per proton transferred:

$$C_{NWD} = \frac{\dot{n}_{H_2O}^{in,an} - \dot{n}_{H_2O}^{out,an}}{\frac{iA}{F}} \quad (1)$$

Therefore, a positive NWD implies an overall water transport from the anode to the cathode. This means electro-osmotic drag dominates transport in the absence of pressure or temperature gradient effects. A negative NWD means the net water movement direction is from the cathode toward the anode, and back diffusion dominates, in the absence of pressure or temperature gradient effects. The NWD directions are labeled in Fig. 1b.

2.3.2. Desiccant method

The average NWD was measured by condensing and collecting the water at the anode outlet. For repeatability, it is highly recommended to condense and collect the water at the cathode outlet as well. That way the NWD is measured and the water mass conservation equation is verified. Therefore for each measurement, the cell outlet streams were condensed and trapped in separate desiccant bottles filled with Dryerite® (anhydrous $CaSO_4$, W.A. Hammond Drierite Co.). The change in bottle mass due to the condensed water was recorded. For the conservation of mass, the amount of water coming in the cell with the gas streams and the amount of water generated during the experiment should be equal to the amount of water collected at the anode and cathode outlets according to

$$m_{H_2O}^{in,an} + m_{H_2O}^{in,cat} + m_{H_2O}^{gen} = m_{H_2O}^{out,an} + m_{H_2O}^{out,cat} \quad (2)$$

where the mass of water generated during the measurement is simply

$$m_{H_2O}^{gen} = \left(\frac{iA}{2F}\right) \cdot M_{H_2O} \cdot \Delta t \quad (3)$$

The galvanostatic operation insures that the rate of water generation is constant and well known. Using the desiccant method, the net water drag coefficient is computed from

$$C_{NWD} = \frac{m_{H_2O}^{in,an} + m_{H_2O}^{out,an}}{\left(\frac{iA}{F}\right) \cdot M_{H_2O} \cdot \Delta t} \quad (4)$$

In all data recorded and presented here, the experimental deviation from the steady state conservation of mass was less than 5%, indicating a true steady state had been achieved and storage/depletion terms were insignificant during measurement.

2.3.3. Real time dew point sensors method

With careful heating of dew point sensors and exit lines, water condensation is prevented and the dew point sensors can be used to compute an instantaneous or average net water drag coefficient. Using the dew point temperature reading at the anode outlet the saturation pressure of the stream can be calculated, and therefore the real-time anode outlet water flow rate can be shown as:

$$\dot{n}_{H_2O}^{out,an} = (\lambda_{H_2} - 1) \frac{iA}{2F} \frac{P_{sat}(T_{dew_{anOut}})}{(P - P_{sat}(T_{dew_{anOut}}))} \quad (5)$$

Similarly, the inlet water vapor flow rate at the anode is calculated, since the anode inlet dew point is an input defined for the experiment and delivered by the calibrated humidification system:

$$\dot{n}_{H_2O}^{in,an} = \lambda_{H_2} \frac{iA}{2F} \frac{P_{sat}(T_{dew_{anIn}})}{(P - P_{sat}(T_{dew_{anIn}}))} \quad (6)$$

The net water drag coefficient from the sensor readings is therefore computed by plugging Eqs. (5) and (6) into Eq. (1). The water amount at the cathode outlet can be computed in a similar fashion to verify that mass is conserved.

3. Results and discussion

The performance curve introduced under baseline conditions is at a cell temperature of 60 °C. After steady operation at 2 A cm⁻² established, the cell temperature was increased in steps while adjusting the dew point to keep the required RH constant. Operation at each temperature lasted for more than 45 min in order to ensure steady state in performance and water transport and storage, as verified by performance and water balance measurements. After steady state operation, water was collected with the desiccant bottles for around 20 min, while the dew point sensors were recording the real time water measurement. After water collection, EIS was performed. The same was repeated after each temperature step until cell operation was not possible due to dry-out. The same experiments at 2 A cm⁻² were performed under each operating condition shown in Table 2.

3.1. Baseline performance curve

Fig. 2 shows the baseline condition performance curve with the corresponding area specific resistance (ASR). The cell temperature

Table 2
Operating conditions for increased temperature experiments.

	Modification to baseline	Purpose
Condition 1	Baseline condition (Table 1)	
Condition 2	Increase of cathode inlet pressure from 180 kPa to 240 kPa	A pressure differential is created across the membrane
Condition 3	Increase of cathode humidity from dry to 53% RH, with a cathode inlet pressure of 240 kPa	More water is added to the cathode side via cathode stream humidification
Condition 4	Increase of cathode humidity from 53% RH to 75% RH, with a cathode inlet pressure of 240 kPa.	An excessively humid inlet cathode stream condition is investigated (75% RH)

is maintained at 60 °C while the hydrogen gas is humidified to 53%, and the cathode inlet is dry. Both anode and cathode sides are pressurized to 180 kPa absolute at the inlet, so the pressure gradient across the membrane is considered negligible. The performance curve at low and medium current densities is typical, with a kinetic drop at very low current densities and an ohmic region characterized by a constant slope at medium current density ($1\text{--}1.5\text{ A cm}^{-2}$). The performance curve does not have an inflection point at high current densities to represent non-linear mass transport loss as commonly observed in channel/land cells [37]. At current densities above 2 A cm^{-2} , the performance curves seems to slightly change slope. This is simultaneous with the linear increase in ASR recorded after 2 A cm^{-2} . The ASR is almost constant below 2 A cm^{-2} . At 2 A cm^{-2} it is slightly lower (44 m Ohm cm^2) than other values and this is attributed to sufficient membrane hydration due to water generation at 2 A cm^{-2} , with the dominance of back diffusion. The increase in ASR after 2 A cm^{-2} is due to the dominance of electro-osmotic and thermo-osmotic [38] drag at such high current densities, which contribute in partially drying out the membrane. At 3 A cm^{-2} ASR is increased to around 50 m Ohm cm^2 . A current density of 2 A cm^{-2} was chosen for temperature step testing since the performance at this point is not limited by mass transport limitations or any dry-out phenomena, and efficiency is still high enough for practical operation.

3.2. Exploring high temperature operation—dry cathode inlet and cathode pressure effect

Two testing conditions have a dry cathode inlet: The baseline condition with a cathode inlet pressure of 180 kPa, and Condition 2 which varies from the baseline conditions by the increase of cathode inlet pressure to 240 kPa, therefore creating a pressure differential across the membrane.

Temperature was increased in steps at 2 A cm^{-2} , as shown in Fig. 3. Under baseline Condition 1, the highest achieved stable operating temperature at 2 A cm^{-2} was 65 °C. The voltage increases from around 570 mV to a little above 590 mV, as the temperature goes from 60 to 65 °C. Looking at the NWD in Fig. 4, we observe that at 60 °C the NWD has a negative value. As the temperature is increased, the NWD becomes less negative and a change in sign of NWD occurs at an intermediate temperature between 62.5 and 65 °C. This means that as the experiment started at 60 °C, the overall net direction of water was back to the anode and dominated by back diffusion. As the temperature increased, the direction of net water transport changed toward the cathode. Also, at the

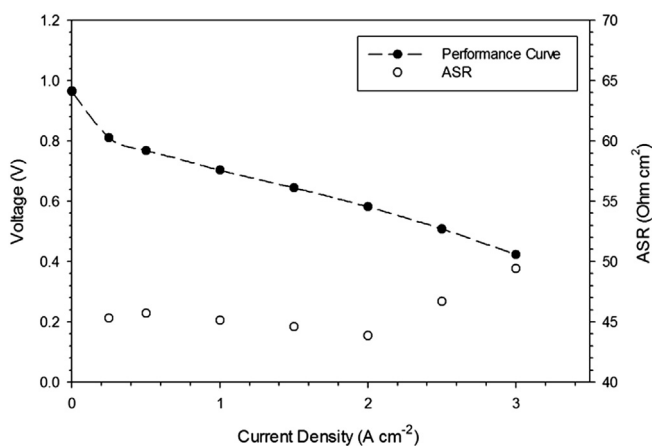


Fig. 2. Performance curve and ASR for baseline conditions at a cell temperature of 60 °C.

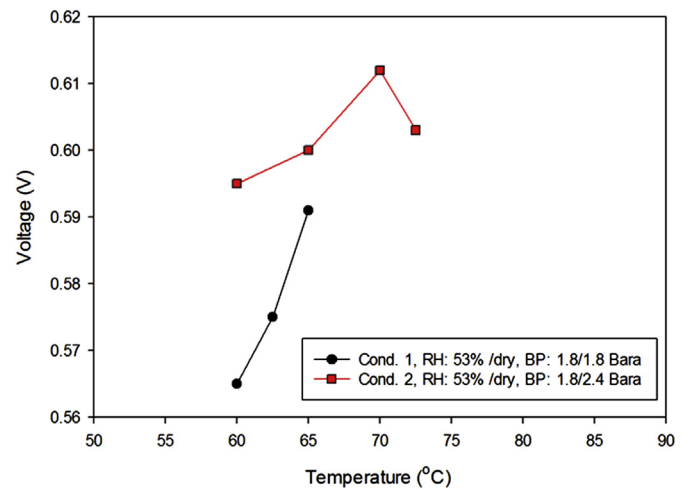


Fig. 3. Cell voltage as a function of temperature with baseline Condition 1, and Condition 2, at 2 A cm^{-2} .

temperature of 65 °C it is clear that the net water direction is from the anode toward the cathode. No data are shown at a temperature higher than 65 °C because the cell could not operate in steady state at 67.5 °C. As previously discussed, Condition 2 is the same as the baseline condition except for an increase of cathode pressure from 180 kPa to 240 kPa to create a pressure differential across the membrane, favoring transport to the anode. The voltage under Condition 2 is also plotted as a function of temperature on Fig. 3. The voltage under Condition 2 is higher than the voltage of the baseline condition, as expected due to the increase of pressure at the cathode. Although the baseline condition did not operate above 65 °C, Condition 2 operates stably at the temperature of 72.5 °C. Voltage increased as temperature increased and peaked at 70 °C. Then it dropped at 72.5 °C, yet remained stable, whereas there was no stable operation at 75 °C. As seen from Fig. 4, the NWD for Condition 2 is almost a perfect negative offset of the NWD from the baseline condition, which is expected due to the linear relationship between pressure differential and convective flux [55]. The more negative NWD reveals that the creation of the pressure differential across the membrane forced more water back from the cathode toward the anode, keeping the membrane hydrated to a higher temperature. An effective permeability of use for models can be

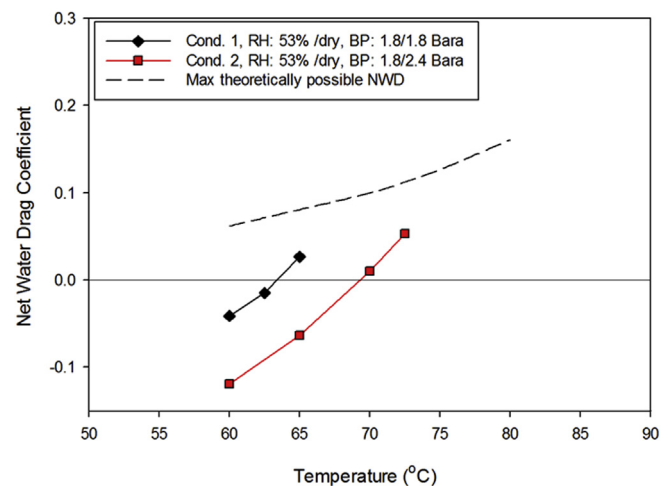


Fig. 4. NWD coefficient evolution as a function of temperature with baseline Condition 1, and Condition 2, at 2 A cm^{-2} .

computed using Eq. (7) in order to describe the negative offset due to the pressure differential:

$$Q = \frac{-KA \Delta P}{\mu L} \quad (7)$$

Q , A , and μ represent the flow rate, cross-sectional area of flow, and viscosity of water respectively. $\Delta P/L$ is the pressure gradient across the membrane having thickness L . K is the effective Darcy permeability. The flow rate Q , can directly be calculated from Eq. (8), and then converted from mol s^{-1} to $\text{m}^3 \text{s}^{-1}$ for consistency:

$$Q = (NWD_{\text{Cond}_2} - NWD_{\text{Cond}_1}) \frac{iA}{F} \quad (8)$$

The computed effective permeability values at each temperature are shown in Table 3, and clearly indicate a linear offset due to the pressure gradient. The effective in-situ permeability averages at $3.64 \times 10^{-20} \text{ m}^2$, which is consistent to the range of values found in literature (between 10^{-20} and 10^{-18} m^2) [56,57].

As temperature increased, the NWD also increased and became less negative, where it eventually changed sign and became slightly positive at the cell temperature of 70°C . At this point, the operation was stable and performance was at peak value. Further increase in temperature elevated the NWD to a more positive value, resulting in anode-dry out and unstable performance.

Fig. 5 represents the transient voltage, ASR and NWD evolution when the temperature reached 67.5°C under the baseline Condition 1. The voltage gradually decreases over a period of less than 7 min until there is no stable operation and the cell shuts down. Simultaneously, the ASR gradually increased. The initial ASR is $48 \text{ m}\Omega \text{ cm}^2$ and the final ASR is $104 \text{ m}\Omega \text{ cm}^2$ right before cell shutdown. The voltage drop with simultaneous ASR increase is a clear indication of membrane dry out. Also on Fig. 5, the evolution of real time NWD reveals an increasingly positive NWD with time evolution concurrent to the voltage drop and ASR increase. This indicates that with time, at 67.5°C and baseline Condition 1, less water is exiting from the anode outlet side of the cell, since the anode inlet is a constant value. An increasing anodic dry out is the reason for gradual voltage drop. The same is true for Condition 2 at 75°C . Impedance spectra for baseline Condition 1 and Condition 2 are plotted in Nyquist format in Fig. 6. The common electric circuit analogy used to deconvolute charge transfer resistances, ASR and mass transport is shown in Fig. 6c [58,59]. ASR and charge transfer resistance deconvoluted from the impedance spectra are shown in Fig. 7 for the different temperatures at 2 A cm^{-2} . For baseline Condition 1, as temperature increases, there is no change in ASR until 65°C . The charge transfer resistance gradually decreases as temperature increases. This is also clearly observed in the reduction of charge transfer arc diameter in Fig. 6a. Even though ASR increased as temperature increased from 62.5 to 65°C , this did not significantly reduce the cell voltage. The cell voltage is more likely to have increased due to the reduction of charge transfer resistance or improved transport, which is already an indication that even though stable operation was limited by membrane conductivity, the performance was dominated by another mechanism. The emphasis on the charge transfer resistance in the interpretation of

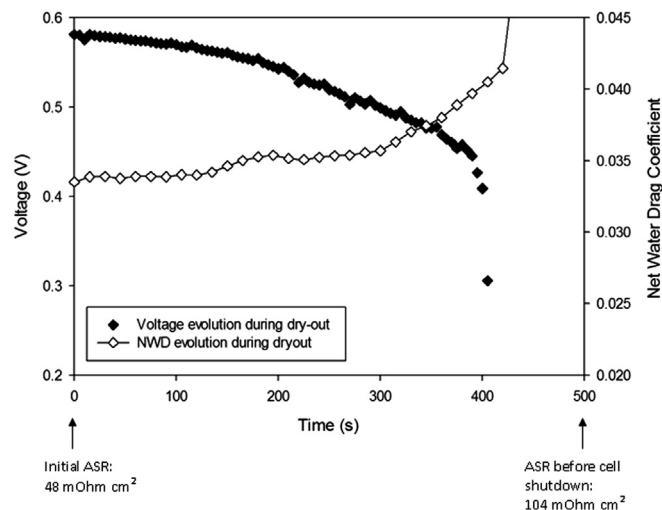


Fig. 5. Evolution of voltage, NWD and ASR during transient dry-out that leads to shutdown of operation at 67.5°C with baseline condition, at 2 A cm^{-2} .

the results comes from the fact that the slight change in water content in the catalyst layer is usually recorded in the high frequency arc as well. This is due to water coverage of catalytic sites or dehydration of ionomers in the case where water content is low in the cathode catalyst layer. The sensitivity of the cell operation to the water content in the catalyst layer is a result of the OME design not limited by mass transport in the flow field or DM. This is due to low water saturation of 0.2 in the DM, as previously explored [37,38] attributed to improved water removal by the OME design, through elimination of conventional lands. This makes the low frequency arc (mass transport) less sensitive to changes in water content since water sites that block oxygen transport are minimal in the GDL and the flow field.

The impedance spectra of Condition 2 are plotted in Fig. 6b, and the deconvoluted charge transfer resistance and ASR are plotted on Fig. 7 along those of baseline condition previously

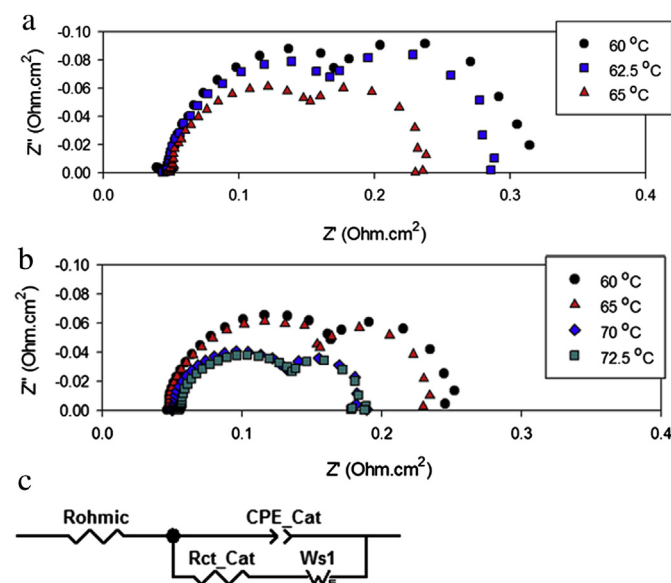


Fig. 6. a) Nyquist plot for baseline Condition 1, b) Nyquist plot for Condition 2, c) electric circuit model used for EIS data fit.

Table 3
Calculated effective water permeability for a pressure differential of 60 kPa.

Temperature ($^\circ\text{C}$)	Effective hydraulic permeability k (m^2)
60	3.46×10^{-20}
62.5	3.42×10^{-20}
65	4.04×10^{-20}
Average: $3.64 \times 10^{-20} \pm 9\%$	

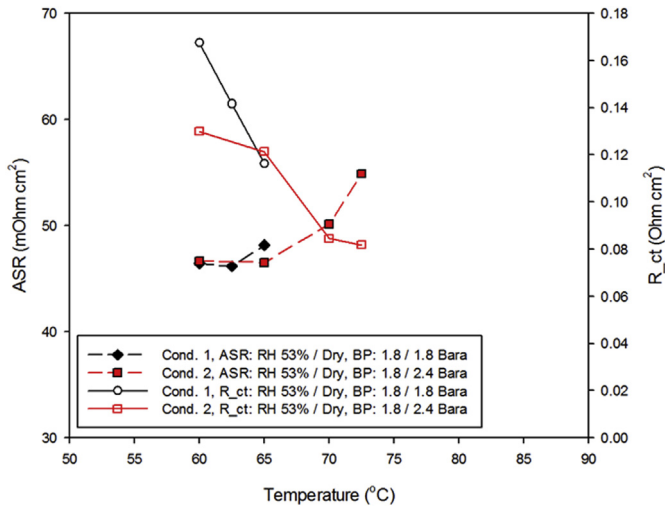


Fig. 7. Charge transfer resistance and ASR data from EIS, for baseline Condition 1, and Condition 2, at 2 A cm^{-2} .

discussed. The ASR trend as a function of temperature is very similar to the one observed for the baseline Condition 1. As the cell temperature increased from 60 to 65 °C, there was no change in ASR. Then as temperature increased from 65 to 72.5 °C, ASR gradually increased. Both Conditions 1 and 2 show a flat ASR followed by a gradual increase. Charge transfer resistance for Condition 2 decreases with increasing cell temperature and almost reaches a plateau. The decrease is small from 60 to 65 °C relative to the decrease in charge transfer resistance from 65 to 70 °C. This is also shown in the slight change in charge transfer arc diameter in Fig. 6b from 60 to 65 °C, followed by a more significant drop in arc dimension between 65 and 70 °C. The increase in ASR is also seen on the Nyquist plot by a shift in the real axis intercept to higher values. We also note that the peak performance at 70 °C corresponds to a slightly positive NWD. The same observation made for the baseline condition can be made for Condition 2 in regard of performance and ASR. There is an increase in performance from 65 to 70 °C even though ASR indicates that the membrane became dryer with increased temperature. Therefore, it is not the membrane hydration that dominates performance over this temperature range, but the state of the catalyst as observed by the behavior of the charge transfer resistance. The mechanism and physics that describe this change in charge transfer resistance are investigated and interpreted in the next section.

3.3. Exploring high temperature operation—effect of cathode humidity

Condition 3 varies from Condition 2 only in the increased humidification of the cathode inlet stream to 53% RH. The pressure gradient across the membrane is the same as Condition 2. The voltage evolution with temperature for Condition 3 is plotted in Fig. 8. Voltage increases from 60 °C to 75 °C and peaks at 75 °C. Voltage decreases after 75 °C but stable operation is possible up to a temperature of 80 °C due to a combined effect of cathode flow humidification and favorable pressure gradient toward the anode. The voltage of Condition 3 is lower when compared to Condition 2, partially due to reduced oxygen mole fraction, and the effect of added humidity on the catalyst layer. Nevertheless operation for Condition 3 is possible at a higher temperature. Even though there is a reduction in gas phase oxygen mole fraction from Condition 2 to Condition 3 due to the added humidity, Eq. (9) can be used to

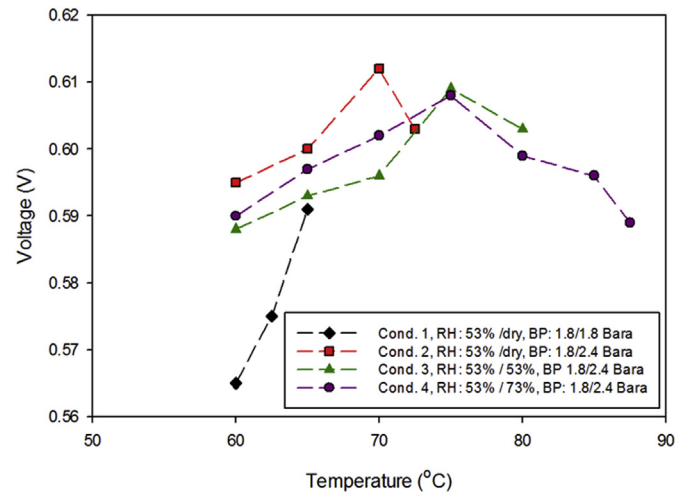


Fig. 8. Cell voltage as a function of temperature under all measured conditions, at 2 A cm^{-2} .

evaluate the impact of reduced oxygen mole fraction on over-potential [60].

$$V_{\text{Cond}_3} - V_{\text{Cond}_2} = \frac{R_u}{F} [T_{\text{Cond}_3} \ln(C_{\text{O}_2,3}) - T_{\text{Cond}_2} \ln(C_{\text{O}_2,2})] \quad (9)$$

Using Eq. (9), the voltage drop calculated, due to the reduced mole fraction of oxygen with the introduction of humidity at the cathode in Condition 3 is expected to be around 2 mV. However, the measured voltage drop varies between 8 mV and 16 mV as shown in Fig. 8. We attribute the additional loss to increased catalyst layer coverage from water with the introduction of humidity.

The NWD coefficient is shown in Fig. 9 and the Nyquist plots from EIS are shown in Fig. 10. The NWD in Fig. 9 confirms that the reason for increased maximum temperature operation is a more negative NWD. This is also shown in the ASR trend in Fig. 11. ASR as a function of temperature in Condition 3 exhibits the same trend as the previous conditions, but the ASR remains constant over a broader temperature range before increasing due to loss of water in the membrane. The charge transfer resistances are shown in Fig. 11. Charge transfer resistances with the humidified cathode are higher than charge transfer resistances of Condition 2 with a dry cathode.

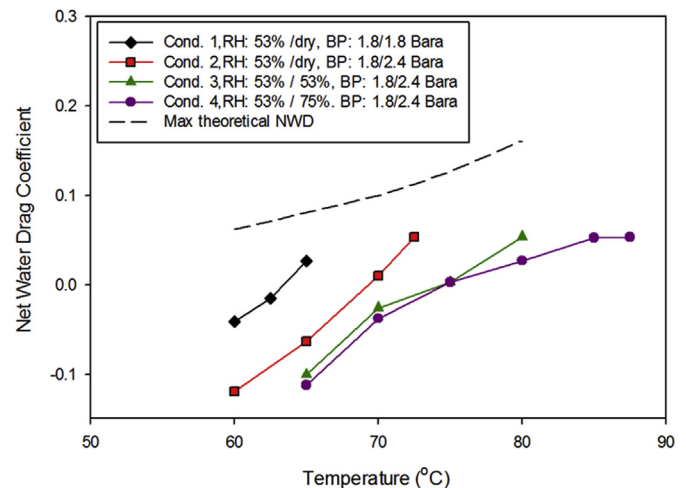


Fig. 9. NWD coefficient as a function of temperature under all measured conditions.

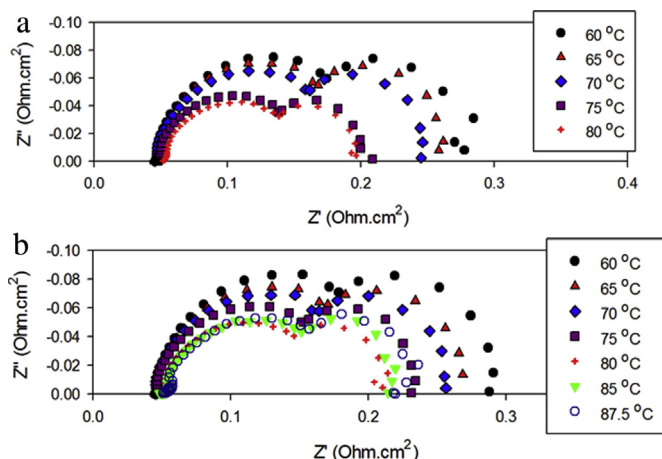


Fig. 10. a) Nyquist plot for Condition 3, b) Nyquist plot for Condition 4.

There is also an increase in mass transport resistance in Condition 3 compared to Condition 2, as shown in Fig. 12.

For Condition 3, we also notice that the peak voltage corresponds to a slightly positive net water drag coefficient and to an ASR value that is higher than the minimum. This again shows that at the maximum stable operating temperature limit is determined by membrane hydration but the performance here is limited at the catalyst level.

Condition 4 varies from Condition 3 by the increase of the cathode inlet RH from 53% to 75%. The voltage evolution with respect to increasing temperature is very similar to what was observed in Condition 3. The peak voltage also occurs at the cell temperature of 75 °C, with an overall voltage trend at 2 A cm⁻² that is slightly higher than that of Condition 3. The voltage in Condition 4 remains lower than that of Condition 2 with a dry cathode. The explanation is the same as the one given in the previous section. A 75% RH cathode inlet increased water in the catalyst layer compared to the dry cathode in Condition 2. In fact, the higher the water content at the cathode inlet, the higher the charge transfer resistance, as shown in Fig. 11. The increased mass transport

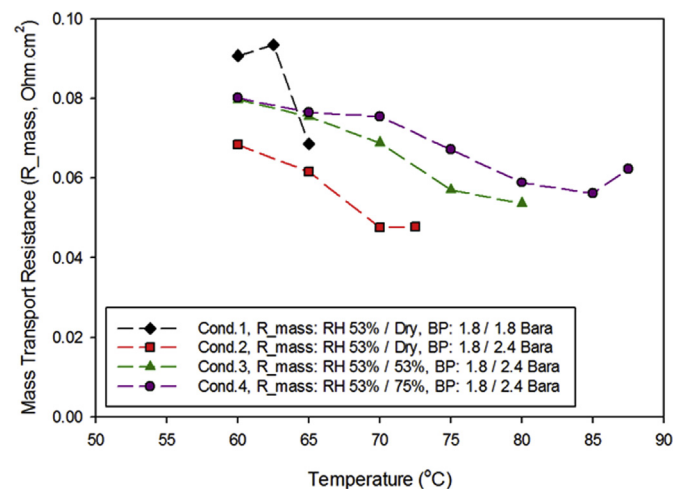


Fig. 12. Calculated mass transport resistances for all measured conditions deduced from EIS data, at 2 A cm⁻².

resistance in Fig. 12 is a clear indication that the increase in charge transfer observed is due to an increase in the water on the catalyst layer. Interestingly, the voltage in Condition 4 is higher than the one observed with Condition 3, even though we see that more water obstructed catalyst activity. The reduced oxygen mole fraction with increased humidity in Condition 4 can only contribute to reduced voltage. Therefore, the increased performance could be partially attributed to better membrane humidification from increase water availability. The ASR values are lowest with a 75% RH, as seen in Fig. 11. This could explain the improved performance compared to a 53% RH cathode inlet humidity. The peak voltage also occurs at a slightly positive NWD as seen in Fig. 9, with a slightly elevated ASR value compared to the minimum.

4. Proposed water mechanism continuum between NWD and performance during dry-out

One can speculate that the maximum performance at a slightly elevated ASR observed is a result of the competition between localized flooding and ionomer dehydration in the catalyst layer (CL). For Conditions 2, 3, and 4, an increase in voltage is visible with increasing temperature, until a peak is reached. This occurred simultaneously with the observed monotonic decrease in charge transfer resistance with increasing temperature, until a drop in charge transfer resistance to a plateau was observed at the temperature for which the highest voltage was recorded at a specific condition. The ASR trend was also consistent, with a flat ASR as a function of temperature followed by a monotonic increase in ASR at the temperature with the highest voltage and lowest charge transfer resistance for a specific conditions set. This increase in ASR also corresponds to the change in NWD direction from anode to cathode. The impact of water addition at the cathode on the charge transfer resistance and mass transport behavior indicates that the phenomenon observed is likely water accumulation in the catalyst layer. The addition of more water (75% RH) increased the charge and mass transport resistances but pushed more water back to the anode and therefore increased membrane hydration at higher temperatures. Fig. 13a is a simplified, not to scale schematic the cathode catalyst layer in agglomerate form next to the membrane. At low temperatures, the high charge transfer resistance due to an excess of liquid water content in the catalyst layer is sketched in Fig. 13b. Excess liquid water in the catalyst layer is the cause of the observed reduced electrochemically active area and increased

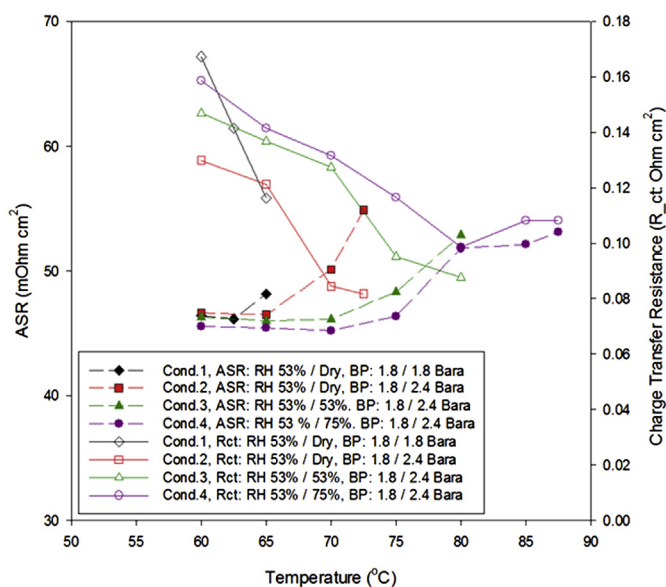


Fig. 11. Charge transfer resistance and ASR data from EIS, for all measured conditions, at 2 A cm⁻².

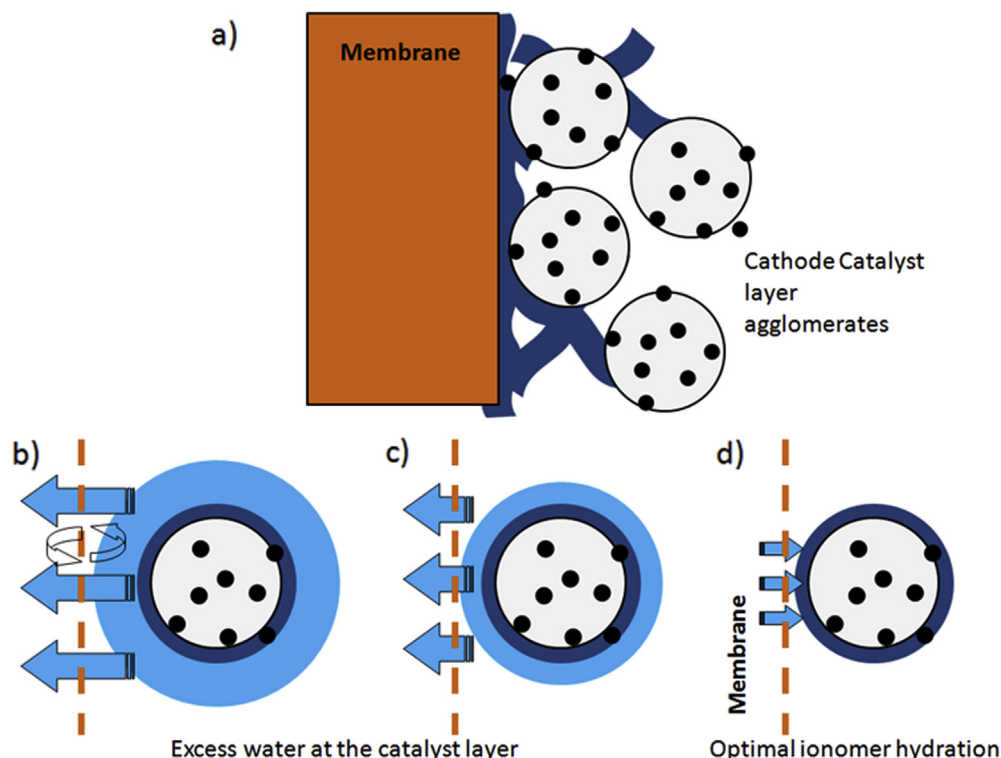


Fig. 13. Cathode catalyst layer hydration state as interpreted from temperature step experiments a) membrane and cathode catalyst layer schematic, b) agglomerate with excess water and back diffusion, c) agglomerate with partially evaporated water film, d) enough water for ionomer hydration only with limited back-diffusion of water.

oxygen diffusion effective resistance. This also provides a negative NWD through enhanced back diffusion, as also shown in Fig. 13 by the arrows. The concentration of liquid water in the cathode catalyst layer is high enough to promote back diffusion and therefore keep a low ASR value. As the temperature increases, the fraction of liquid water in the cathode catalyst layer is reduced as represented in Fig. 13c. More catalyst active area is cleared therefore the charge transfer resistance is reduced, mass transport is improved for oxygen, and performance has increased. This same reduction in liquid water content results in a lower back diffusion and therefore a less negative NWD, represented by the smaller arrow. NWD is still negative at this point and provides enhanced membrane hydration, as shown by the flat ASR with the initial increase in temperature under a specific operating condition. As temperature is increased, the liquid water fraction in the cathode catalyst layer is further reduced to the point where most catalytic active areas are cleared, and the hydration is optimal. There is a correct amount of liquid water to keep the ionomer of the cathode catalyst layer hydrated and highly conductive to ions, with minimal excess water is present to block the active sites and hinder oxygen permeation. This optimal cathode catalyst hydration is observed with the abrupt drop in charge transfer resistance at a specific temperature and a peak in the performance. The NWD at this condition is slightly positive, and beyond this critical value, anode dry-out is initiated.

As inlet humidity is increased at the cathode, the drop in charge transfer resistance (the transition from Fig. 13c to d) occurs at a more elevated temperature. This is another indication that the kinetic activity at the cathode catalyst layer that is being interpreted through charge transfer deconvolution from EIS data. At this critical cathode catalyst hydration, the liquid water concentration is not high enough to promote back diffusion of liquid water from the cathode to the membrane. Therefore the net water movement becomes from the anode to the cathode as observed by the measured positive NWD and indicated by the direction of the

arrows in Fig. 13d. This triggers the increase in ASR due to anodic dry-out that is now dominated by electro-osmotic drag due to reduced back diffusion. As temperature is further increased, electro-osmotic drag leads to anodic dehydration to a point where operation is not possible, due to the very high electric resistance induced in the membrane. These results indirectly show a linkage between cathode CL liquid water content and maximum operating temperature, through the mechanism of enhanced back diffusion with liquid availability.

5. Conclusions

A comprehensive examination of net water movement, ASR and EIS data were used to understand the origins of performance and operation limitations and enable high temperature operation suitable for automotive application at high current density (2 A cm^{-2}) of a PEFC using a porous open metallic element (OME) flow field. Operation at ultra-high current density (3 A cm^{-2}) is possible. For the OME architecture, the limiting factor for high power operation at elevated temperatures suitable for automotive operation is anodic dry-out triggered by electro-osmotic drag as a result of improved water evacuation from the cathode. Results indicated a coupling between the availability of liquid in the catalyst layer and maintaining stable high temperature operation. As temperature was increased at any specific operating condition, voltage increased since more catalyst areas were cleared, as long as the net water drag (NWD) was toward the anode. After the maximum voltage peak, a further increase in temperature resulted in a net water movement toward the cathode, gradually drying out the anode side of the membrane. This anodic dry out resulted in an increased ASR and reduction of voltage. When ASR reached a high value due to excess dry-out, steady operation at high temperature was not possible and a transient voltage drop was recorded until cell shutdown. The increase in cathode pressure and cathode inlet

relative humidity increased maximum temperature for which stable operation is possible (from 60 °C to 90 °C) for the conditions tested. At a 0.6 bar differential pressure across the membrane, an effective hydraulic permeability of $3.64 \times 10^{-20} \text{ m}^2$ was measured. This is due to a more negative net water drag caused by improved back diffusion. The trade-off between liquid water overshadowing cathode catalyst sites and its contribution in promoting back diffusion is identified as key in the design for anodic dry-out limited operation.

Acknowledgments

The authors would like to thank Amedeo Conti from Nuvera Fuel Cells Inc. for many helpful discussions and guidance. This work is funded by the United States Department of Energy (DOE) Energy Efficiency and Renewable Energy (EERE) Program through Nuvera Fuel Cells Inc. under contract number DE-EE0000472.

References

- [1] Toyota Motors Co, Toyota Confirms Hydrogen Fuel-Cell Sedan Due Out in 2015 (Press release) Detroit, MI. (8 August 2012). Retrieved from: <http://www.insideline.com/toyota/toyota-confirms-hydrogen-fuel-cell-sedan-due-out-in-2015.html>
- [2] Toyota Motors Co. Detroit Auto Show, Toyota: \$50,000 Fuel Cell Sedan on Track to Launch in 2015, or Sooner (Press release) (2012). Retrieved from: <http://green.autoblog.com/2011/01/14/toyota-fuel-cell-sedan-on-track-for-2015/>.
- [3] Nissan Motor Co., By 2016 [...] All-New Fuel Cell Electric Vehicle (FCEV) Together With Strategic Partner, Daimler (Press release), Japan. Retrieved from: <http://green.autoblog.com/2011/11/29/nissan-fuel-cell-vehicle-on-track-for-2015/>.
- [4] General Motors, We do Believe Fuel Cells can be Commercialized by (the) 2015/2016 Time Frame (Press release), Detroit MI. Retrieved from: <http://www.earthtechling.com/2012/09/gm-keeps-2015-in-its-sights-for-fuel-cell-vehicles/>.
- [5] T.A. Zawodzinski, T.E. Springer, F. Uribe, S. Gottesfeld, Solid State Ionics 60 (1993) 199.
- [6] M.L. Perry, J. Newman, E.J. Cairns, J. Electrochem. Soc. 145 (1998) 5.
- [7] T.E. Springer, S. Gottesfeld, Electrochem. Soc. Proc. 197 (1991) 232.
- [8] M. Eikerling, A.A. Kornyshev, J. Electroanal. Chem. 453 (1998) 89.
- [9] H. Li, Y. Tang, Z. Wang, Z. Shi, S. Wu, D. Song, J. Zhang, K. Fatih, J. Zhang, H. Wang, Z. Liu, R. Abouattallah, A. Mazza, J. Power Sources 178 (2008) 103.
- [10] X. Li, I. Sabir, Int. J. Hydrogen Energy 30 (2005) 359.
- [11] A. Pollegri, P.M. Spaziant, US Patent No. 4,197,178 (1980).
- [12] F. Spurrier, B. Pierce, M. Wright, US Patent No. 4,631,239 (1986).
- [13] S. Granata, B. Woodle, US Patent No. 4,684,582 (1987).
- [14] D. Jeon, S. Greenway, S. Shimpalee, J. Van Zee, Int. J. Hydrogen Energy 33 (2008) 1052.
- [15] G. Hu, J. Fan, S. Chen, Y. Liu, K. Cen, J. Power Sources 136 (2004) 1.
- [16] L. Wang, H. Liu, J. Power Sources 134 (2004) 185.
- [17] C. Cavalca, S. Homeyer, E. Walsworth, US Patent No. 5,686,199 (1997).
- [18] N. Pekula, K. Heller, P. Chuang, A. Turhan, M.M. Mench, J. Brenizer, K. Unlu, Nucl. Instrum. Methods Phys. Res. 542 (2005) 134.
- [19] T. Trabold, J. Owejan, D. Jacobson, M. Arif, P. Huffman, Int. J. Heat Mass Transf. 49 (2006) 4712.
- [20] A. Kazim, H.T. Liu, P. Forges, J. Appl. Electrochem. 43 (1999) 1409.
- [21] A. Turhan, S. Kim, M.C. Hatzell, M.M. Mench, Electrochim. Acta 55 (2010) 2734.
- [22] P. Owejan, T.A. Trabold, D.L. Jacobson, M. Arif, S.G. Kandlikar, Int. J. Hydrogen Energy 32 (2007) 4489.
- [23] S. Litster, C. Buie, T. Fabian, J. Eaton, J. Santiago, J. Power Sources 154 (2007) 1049.
- [24] G. Velayutham, J. Kaushik, N. Rajalakshmi, K.S. Dhathathreyan, Fuel Cells 07 (2007) 314. Wiley-VCH.
- [25] G. Park, Y. Sohn, T. Yang, Y. Yoon, W. Lee, C. Kim, J. Power Sources 131 (2004) 182.
- [26] M.P. Manahan, M.M. Mench, J. Electrochem. Soc. 159 (2012) F322.
- [27] H. Markötter, R. Alink, J. Haußmann, K. Dittmann, T. Arlt, F. Wieder, C. Tötzke, M. Klages, C. Reiter, H. Riesemeier, J. Scholta, D. Gerteisen, J. Banhart, I. Manke, Int. J. Hydrogen Energy 37 (2012) 7757.
- [28] M.P. Manahan, M.C. Hatzell, E.C. Kumbur, M.M. Mench, J. Power Sources 196 (2011) 5573.
- [29] M.S. Wilson, C. Zawodzinski, US Patent No. 6,207,310 B1, 2001.
- [30] M.S. Wilson, C. Zawodzinski, US Patent No. 6,037,072, 2000.
- [31] M.S. Wilson, C. Zawodzinski, US Patent No. 5,798,187, 1998.
- [32] M.S. Wilson, US Patent No. 5,641,586, 1997.
- [33] S. Arisetty, A.K. Prasad, S.G. Advani, J. Power Sources 165 (2007) 49.
- [34] T. Shudo, S. Naganuma, Soc. Automot. Eng. 39 (2011) 7261.
- [35] A. Kumar, R.G. Reddy, J. Power Sources 113 (2003) 54.
- [36] B.T. Tsai, C.J. Tseng, Z.S. Liu, C.H. Wang, C.I. Lee, C.C. Yang, S.K. Lo, Int. J. Hydrogen Energy 37 (2012) 13060.
- [37] A.K. Srouji, L.J. Zheng, R. Dross, A. Turhan, M.M. Mench, J. Power Sources 218 (2012) 341.
- [38] L.J. Zheng, A.K. Srouji, A. Turhan, M.M. Mench, J. Electrochem. Soc. 159 (2012) F267.
- [39] M. Eikerling, Y.I. Kharkats, A.A. Kornyshev, Y.M. Volkovich, J. Electrochem. Soc. 145 (1998) 2684.
- [40] B.S. Pivovar, Polymer 47 (2006) 4194.
- [41] T.A. Zawodzinski, S. Radzinski, R.J. Sherman, V.T. Smith, T.E. Springer, S. Gottesfeld, J. Electrochem. Soc. 140 (1993) 1041.
- [42] T.A. Zawodzinski, J. Davey, J. Valerio, S. Gottesfeld, Electrochim. Acta 40 (1995) 297.
- [43] A.B. LaConti, A.R. Fragala, J.R. Boyack, S. Srinivasan, E.G. Will, Proceedings of the Symposium on Electrode Materials and Processes for Energy Conversion and Storage, 77 (1977) 354.
- [44] T.F. Fuller, J. Newman, J. Electrochem. Soc. 139 (1992) 1332.
- [45] G. Xie, T. Okada, J. Electrochem. Soc. 142 (1995) 3057.
- [46] X. Ren, W. Henderson, S. Gottesfeld, J. Electrochem. Soc. 144 (1997) L267.
- [47] S. Kim, M.M. Mench, J. Membr. Sci. 328 (2009) 113.
- [48] M. Tasaka, T. Hirai, R. Kiyono, Y. Aki, J. Membr. Sci. 71 (1992) 151.
- [49] J.P.G. Villaluenga, B. Seoane, V.M. Barragan, C. Ruiz-Bauza, J. Membr. Sci. 274 (2006) 116.
- [50] R. Zaffou, S.Y. Jung, H.R. Kunz, J.M. Fenton, Electrochem. Solid-State Lett. 9 (2006) A418.
- [51] R. Bradean, H. Haas, K. Eggen, C. Richards, T. Vrba, ECS Trans. 3 (1) (2006) 1159.
- [52] DOE, Fuel Cell Technologies Program, Multi-Year Research and Development Plan (2011). http://www1.eere.energy.gov/hydrogenandfuelcells/myrpp/pdfs/fuel_cells.pdf.
- [53] S. Jung, S. Kim, M. Kim, Y. Park, T. Lim, J. Power Sources 170 (2007) 324.
- [54] D. Jeon, K. Kim, S. Baek, J. Nam, Int. J. Hydrogen Energy 36 (2011) 2499.
- [55] M.M. Mench, Fuel Cell Engines, Wiley and Sons, 2008.
- [56] D.M. Bernardi, M.W. Verbrugge, J. Electrochem. Soc. 139 (1992) 2477.
- [57] F. Meier, G. Eigenberger, Electrochim. Acta 49 (2004) 1731.
- [58] D. Malevich, E. Halliop, A.B. Peppley, G.J. Pharoah, K. Karan, J. Electrochem. Soc. 156 (2009) B216.
- [59] N. Fouquet, C. Doulet, C. Nouillant, G. Dauphin-Tanguy, B. Ould-Bouamama, J. Power Sources 159 (2006) 905.
- [60] H.A. Gasteiger, W. Gu, R. Makharia, M.F. Mathias, B. Sompalli, Wiley VCH, New York, 2003, p. 593.